



34 for use in next-generation non-volatile memory because this transition corresponds  
35 to different resistive states.<sup>2</sup> Such materials can mimic neural synapses, which is  
36 essential in neuromorphic computing where devices emulate the human brain.<sup>3</sup> A  
37 gradual, analog variation in resistance near the MIT provides a means to model  
38 synaptic plasticity, achievable with materials that show progressive, voltage-dep-  
39 endent resistance changes.<sup>4</sup> Materials with MIT also hold promise in electronics  
40 beyond memory applications. They have the ability to replace conventional transis-  
41 tors in field-effect transistors (FETs), potentially enhancing energy efficiency and  
42 making the way for ultra-low-power computing.<sup>5</sup> The sharp MIT in materials like  
43 VO<sub>2</sub> at specific temperatures can be used in thermal switches for managing heat  
44 flow in electronics.<sup>6</sup> These materials can act as thermal insulators below the transition  
45 temperature and as thermal conductors above it. A sharp MIT, which is associated  
46 with changes in crystal structure, may also exhibit changes in optical properties.<sup>7</sup>  
47 This property may be exploited to construct optical sensors and smart windows  
48 that can automatically modulate light of a certain frequency. Oxides undergoing  
49 MIT without concurrent magnetic transitions are promising candidates for spin-  
50 -based quantum applications, where control over electronic phases without pertur-  
51 bing spin order is advantageous.<sup>8</sup> Some materials exhibit a high Seebeck coeffi-  
52 cient near the MIT temperature that can be useful for thermoelectric applications.<sup>9</sup>  
53 This could enable the development of efficient thermoelectric generators for waste  
54 heat recovery, enhancing energy efficiency across various industries.

55 Materials undergoing an MIT have attracted significant interest due to the  
56 abrupt, reversible modulation of their properties. Among these, vanadium dioxide  
57 (VO<sub>2</sub>) is a premier candidate for next-generation smart windows, thermal switches,  
58 and energy-responsive devices. Interest in VO<sub>2</sub> is driven particularly due to its  
59 fully reversible structural and electronic transition occurring at a near-ambient  
60 temperature of approximately 68 °C.

61 Vanadium dioxide possesses many possible crystalline forms or polymorphs,  
62 some of which are stable, and others metastable. These include VO<sub>2</sub>(M), VO<sub>2</sub>(R),  
63 VO<sub>2</sub>(A), VO<sub>2</sub>(B), VO<sub>2</sub>(C), VO<sub>2</sub>(D) and VO<sub>2</sub> (paramontroseite).<sup>10</sup> Out of these,  
64 the MIT is associated with the transition between the metallic VO<sub>2</sub>(R) phase above  
65 68 °C and the insulating VO<sub>2</sub>(M) phase below 68 °C. Many techniques have been  
66 used for VO<sub>2</sub> synthesis, including the sol–gel method,<sup>11</sup> magnetron sputtering,<sup>12</sup>  
67 chemical vapor deposition<sup>13</sup> and the hydrothermal method.<sup>10,14</sup> Among these, the  
68 hydrothermal method is known to have minimal environmental impact and is often  
69 employed to synthesize the metastable VO<sub>2</sub>(B) phase. Vanadium pentoxide and  
70 ammonium metavanadate (NH<sub>4</sub>VO<sub>3</sub>) are commonly used vanadium sources in the  
71 hydrothermal synthesis of VO<sub>2</sub>. Commonly used reducing agents include oxalic  
72 acid,<sup>15</sup> hydrazine hydrate,<sup>16</sup> ethylene glycol,<sup>17</sup> octadecyl amine,<sup>18</sup> citric acid,<sup>16</sup>  
73 formic acid<sup>19</sup> and formaldehyde.<sup>20</sup> Out of these, oxalic acid has been the most  
74 preferred reductant in the hydrothermal synthesis of VO<sub>2</sub> due to its low toxicity

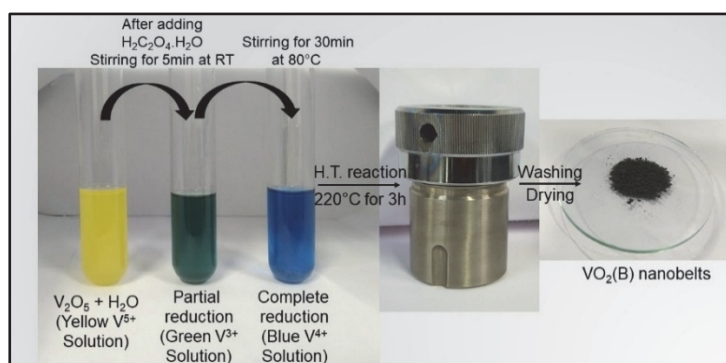
75 and ease of use. Zhu *et al.*<sup>15</sup> reported the synthesis of several types of VO<sub>2</sub>(B)  
76 nanostructures by a hydrothermal reaction combining (NH<sub>4</sub>VO<sub>3</sub>) and oxalic acid  
77 at different times and temperatures. The resulting products had combinations of  
78 nanorods, nanoflakes and nanoflowers with the concentration of oxalic acid influ-  
79 encing their proportions.<sup>15</sup>

80 In this paper, we report a simple method for the preparation of VO<sub>2</sub>(M) *via*  
81 heat treatment of hydrothermally derived VO<sub>2</sub>(B). The effect of different annealing  
82 conditions on the final products was characterized using X-ray diffraction (XRD),  
83 Raman spectroscopy, scanning electron microscopy (SEM) and UV-Vis spectro-  
84 scopy, while the thermochemical properties were studied using differential scan-  
85 ning calorimetry (DSC).

## 86 EXPERIMENTAL

### 87 *Synthesis of VO<sub>2</sub>(B)*

88 We synthesized VO<sub>2</sub>(B) by a hydrothermal reaction between commercial vanadium pent-  
89 oxide powder and oxalic acid. Firstly, 0.73 g of V<sub>2</sub>O<sub>5</sub> (1 mmol) was added to a beaker containing  
90 40 mL deionized water. This mixture was stirred under ambient conditions for 5 min using a  
91 magnetic stirrer. Then, 1.51 g of H<sub>2</sub>C<sub>2</sub>O<sub>4</sub>·H<sub>2</sub>O (3 mmol) was added to it and further stirred for  
92 5 min, yielding a green solution indicating partial reduction. This solution was continuously  
93 stirred at 80 °C until the aqueous solution turned into a clear, transparent dark blue color. The  
94 change in color implied a reduction of vanadium from V<sup>5+</sup> to V<sup>4+</sup>. Then, this solution was trans-  
95 ferred into a Teflon<sup>®</sup>-lined stainless-steel autoclave, which was kept in a preheated oven (at 220  
96 °C) for 3 h to complete the hydrothermal reaction for a duration of 3 h. The resulting bluish-  
97 black colored precipitate was separated by centrifugation. This precipitate was then washed  
98 with ethanol and DI water several times to remove any contamination and was dried for 12 h at  
99 60 °C in an oven. This yielded black colored vanadium dioxide powder (henceforth referred to  
100 as S-22). The resulting powder was subsequently ground in a mortar and pestle and subjected  
101 to annealing in a tube-furnace at various temperatures. Fig. 1 illustrates the various steps invol-  
102 ved in the synthesis of vanadium oxide nanobelts.



103  
104  
105

Fig. 1. Schematic illustration of the entire reaction mechanism during hydrothermal synthesis of VO<sub>2</sub> nanobelts.

106 *Synthesis of VO<sub>2</sub>(M)*

107 VO<sub>2</sub>(M) was derived from VO<sub>2</sub>(B) through a controlled annealing process. A 500 mg  
108 sample from the as-synthesized VO<sub>2</sub> (S-22) was taken and annealed at different temperatures,  
109 namely 300, 350, 400 and 450° C (henceforth addressed as S-30, S-35, S-40 and S-45, respect-  
110 ively) for 30 min in a quartz-tube vacuum furnace under low vacuum (10<sup>-2</sup> mbar). Both the  
111 heating and cooling rates were maintained at 5 °C/min.

112 *Characterization*

113 The crystal structure of the powder samples was characterized by XRD (Rigaku-D/MAX-  
114 -RB) with CuK $\alpha$  radiation ( $\lambda = 0.154$  nm). The data were analyzed using SMARTLab software.  
115 The samples were scanned over a  $2\theta$  range of 15–60°. Additionally, chemical and phase analysis  
116 were performed using a Raman spectrometer (Horiba, LabRAM) with a 633 nm laser excitation  
117 source. The microstructure and surface morphology of the sample were examined using field-  
118 -emission SEM (FE-SEM, Jeol). Differential scanning calorimetry (DSC, TA Instruments,  
119 model 2910) studies were performed to investigate phase transition behavior over a temperature  
120 range of 15–100 °C using heating and cooling rates of 10 °C/min. Optical transmittance mea-  
121 surements were carried out using a UV–Vis spectrometer (Ocean Insights) in the wavelength  
122 range of 200–800 nm to evaluate the optical properties of the material.

123

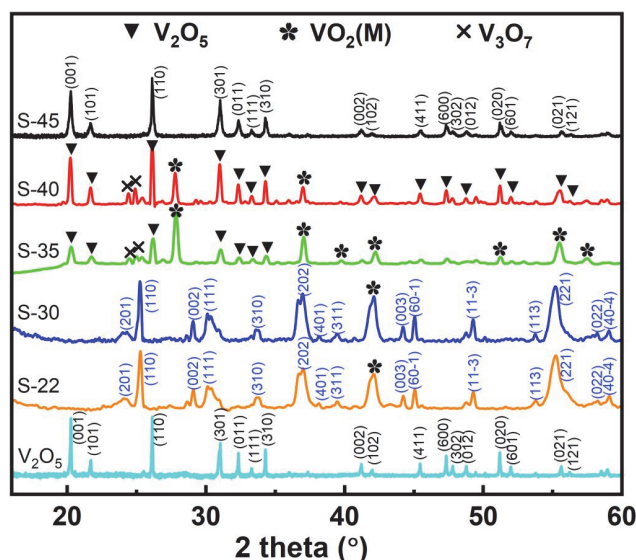
## RESULTS AND DISCUSSION

124 *Structural studies*

125 The crystalline phase and purity of the precursor, as-prepared and annealed  
126 samples were determined by XRD and obtained results are shown in Fig. 2. The  
127 V<sub>2</sub>O<sub>5</sub> spectrum is that of the precursor used for synthesis. The XRD patterns are  
128 readily assigned to V<sub>2</sub>O<sub>5</sub> (ICDD: 09-0387), which reveals the purity of the pre-  
129 cursor. S-22 shows peaks that are in close agreement with the VO<sub>2</sub>(B) phase with  
130 Miller indices (*hkl* planes) indicating growth of the monoclinic VO<sub>2</sub>(B) phase  
131 (ICDD: 01-84-7141). The lattice parameter values calculated are as follows:  $a =$   
132  $= 12.04$  Å,  $b = 3.68$  Å and  $c = 6.43$  Å and it shows *C2/m* space group symmetry,  
133 with the strongest peaks at  $2\theta$  25.28, 29.09, 30.13, 37.01, 49.28 and 55.24°  
134 corresponding to (110), (002), (111), (202), (11 $\bar{3}$ ) and (221) planes, respectively.  
135 Additionally, VO<sub>2</sub>(B) also exhibits a high degree of crystallinity, evidenced by the  
136 well-defined and strong XRD peaks. The diffraction peak at  $2\theta$  42.2° is indexed to  
137 the VO<sub>2</sub>(M) phase (ICDD: 01-076-0456) for the (21 $\bar{2}$ ) plane. There is no evidence  
138 of diffraction peaks corresponding to secondary oxide phases, such as V<sub>2</sub>O<sub>5</sub>. These  
139 results confirm that the VO<sub>2</sub>(B) phase is predominant, with no secondary oxides  
140 detected within XRD resolution limits. S-30 remains predominantly VO<sub>2</sub>(B), with  
141 trace reflections indicating the onset of the phase transition to VO<sub>2</sub>(M).

142 From the analysis of the XRD data, we observe that annealing the sample S-35  
143 at 350 °C resulted in the formation of a predominantly monoclinic VO<sub>2</sub>(M) phase,  
144 with minor secondary phases of V<sub>2</sub>O<sub>5</sub> and V<sub>3</sub>O<sub>7</sub>. The lattice constants are  $a = 5.75$   
145 Å,  $b = 4.54$  Å and  $c = 5.38$  Å, indicating a monoclinic structure with *P2<sub>1</sub>/c* space  
146 group symmetry. The peaks detected at  $2\theta$  27.79, 37.01, 39.72, 42.20, 51.24, 55.45

147 and 57.33° are assigned to the (001), (21 $\bar{1}$ ), (020), (21 $\bar{2}$ ), (22 $\bar{1}$ ), (220) and (022)  
 148 planes, respectively, for the monoclinic VO<sub>2</sub>(M) phase (ICDD: 01-076-0456).



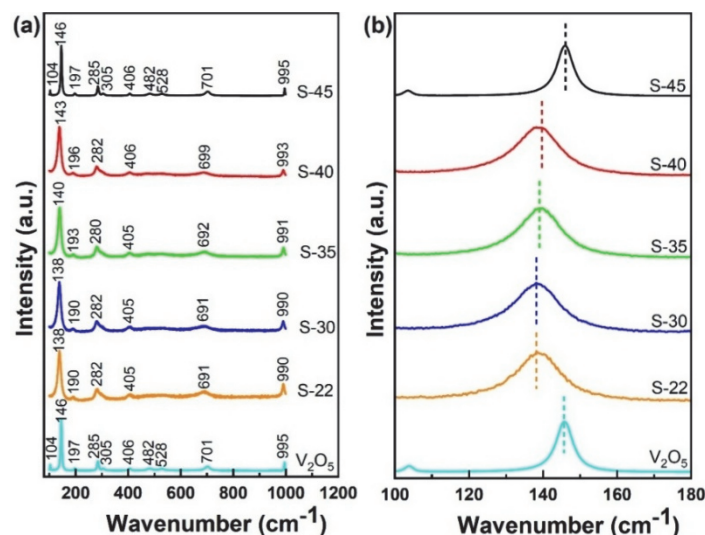
149  
 150  
 151

Fig. 2. XRD patterns of pristine V<sub>2</sub>O<sub>5</sub>, the hydrothermally synthesized sample (S-22) and samples annealed at various temperatures (S-30, S-35, S-40 and S-45) for 30 min.

152 The XRD patterns of sample S-40 are a combination of phases with the pre-  
 153 sence of both VO<sub>2</sub> (M) and peaks belonging to V<sub>2</sub>O<sub>5</sub> and V<sub>3</sub>O<sub>7</sub> (ICDD: 042-0876).  
 154 It can be noted that with the increase in annealing temperature, the intensities of  
 155 the peaks of VO<sub>2</sub>(M) decrease while the intensities of the V<sub>2</sub>O<sub>5</sub> peaks increase,  
 156 showing reduced thermal stability of the VO<sub>2</sub> phase at elevated temperatures. In  
 157 contrast, the XRD spectra of S-45 show complete oxidation of VO<sub>2</sub> to V<sub>2</sub>O<sub>5</sub>, which  
 158 agrees well with existing literature.<sup>21,22</sup> This indicates that during high-tempera-  
 159 ture treatment, metastable VO<sub>2</sub> may have oxidized and transformed into its most  
 160 thermodynamically stable phase, V<sub>2</sub>O<sub>5</sub> (ICDD: 09-0387), which is the same as the  
 161 precursor used for VO<sub>2</sub> synthesis. The average crystallite sizes estimated using  
 162 Scherrer's formula for samples S-22, S-30, S-35, S-40 and S-45 are 19, 22, 24, 31  
 163 and 31 nm, respectively.

164 Raman spectroscopy was used to analyze the structural and phase information  
 165 in addition to XRD. Raman spectra of S-22, the precursor V<sub>2</sub>O<sub>5</sub> and the annealed  
 166 samples are shown in Fig. 3a and b. Characteristic peaks at 146 and 197 cm<sup>-1</sup> are  
 167 consistent with orthorhombic V<sub>2</sub>O<sub>5</sub>, indicating high purity and crystallinity of the  
 168 precursor. The Raman modes at 285 and 406 cm<sup>-1</sup> correspond to the bending  
 169 modes of V=O bonds, and the one at 482 cm<sup>-1</sup> is attributed to the bending of

170 V–O–V bonds. The peaks at 528 and 701  $\text{cm}^{-1}$  are attributed to V–O bonds (com-  
 171 bined stretching and bending vibrations). The 995  $\text{cm}^{-1}$  peak arises from the  
 172 stretching of the V=O bond.<sup>23–25</sup>



173  
 174 Fig. 3. Raman spectra of all samples: a) full spectra and b) Raman spectra in the range of  
 175 135–150  $\text{cm}^{-1}$  highlighting the peak shift.

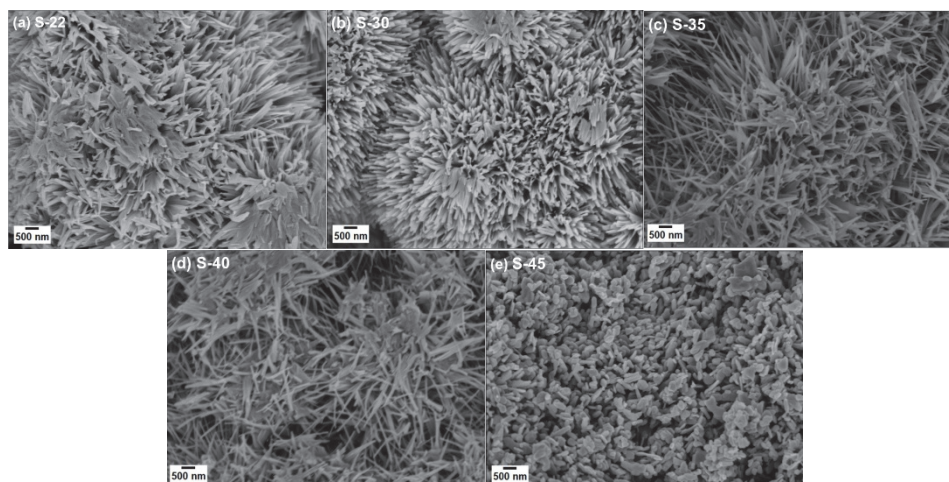
176 Furthermore, the Raman spectrum of the hydrothermally synthesized  $\text{VO}_2(\text{B})$   
 177 phase (S-22) exhibits broad peaks at 138, 190, 282, 405, 691 and 990  $\text{cm}^{-1}$ . The  
 178 peaks at 138 and 282  $\text{cm}^{-1}$  are attributed to V–O–V bending vibrations, while the  
 179 405  $\text{cm}^{-1}$  peak corresponds to V–O–V stretching. The band at 691  $\text{cm}^{-1}$  is associated  
 180 with the coordination of three oxygen atoms around a vanadium center, and the  
 181 strong peak at 990  $\text{cm}^{-1}$  arises from V=O stretching vibrations. According to  
 182 Cheng *et al.*<sup>26</sup> and Zhang *et al.*,<sup>27</sup> the above Raman peaks can be indexed to vibra-  
 183 tional bands of the  $\text{VO}_2(\text{B})$  phase.

184 The sample S-30 exhibits characteristics similar to  $\text{VO}_2(\text{B})$ , indicating the  
 185 stability of the phase up to this temperature. For the samples S-35 and S-40, we  
 186 observe a shift in peaks to higher frequencies (140, 280 and 692  $\text{cm}^{-1}$ ), indicating  
 187 the formation of mixed phases and partial oxidation of  $\text{VO}_2(\text{M})$ . Finally, for the  
 188 sample S-45, the Raman spectrum exhibits sharp peaks identical to those of the  
 189 original  $\text{V}_2\text{O}_5$  precursor, indicating complete oxidation. The zoomed region  
 190 between 135–150  $\text{cm}^{-1}$  (Fig. 3b) provides insights into peak shifts and the phase  
 191 transition from  $\text{VO}_2(\text{B})$  to  $\text{VO}_2(\text{M})$ . Thus, the development of the Raman bands  
 192 corresponds well with the structural changes established using XRD and demon-  
 193 strates the sensitivity of Raman spectroscopy for characterizing the long-range  
 194 order and local structural changes.

195 A detailed analysis of the Raman spectra for samples S-35 and S-40, which  
196 consist of mixed phases of VO<sub>2</sub>(M) and V<sub>2</sub>O<sub>5</sub>, indicates that these phases cannot  
197 be distinctly resolved *via* Raman spectroscopy due to the overlap in their charac-  
198 teristic vibrational modes. Thus, phase identification in this case needs to be done  
199 from X-ray diffraction (XRD) data. Additionally, the Raman spectrum of sample  
200 S-45 exhibits features consistent with V<sub>2</sub>O<sub>5</sub>, indicating a phase transformation from  
201 VO<sub>2</sub> to V<sub>2</sub>O<sub>5</sub>, and closely matches the spectral signature of the V<sub>2</sub>O<sub>5</sub> precursor.  
202 Raman spectroscopy thus serves as a complementary technique to XRD, confirm-  
203 ing that our simple synthesis method reliably produces VO<sub>2</sub> with MIT behavior.

#### 204 *Morphological studies*

205 The morphology of VO<sub>2</sub> nanostructures was analyzed using SEM. Fig. 4  
206 shows the SEM images of the as-grown and annealed vanadium oxide nanostruc-  
207 tures. For the samples S-22, shown in Fig. 4a, multiple nanobelts are connected at  
208 the bottom and spread radially towards the top to form an urchin-like unit.



210  
211 Fig. 4. SEM images illustrating the morphology of the nanostructure samples: a) S-22,  
212 b) S-30, c) S-35, d) S-40 and e) S-45.

213 The width of the nanobelts in the as-grown samples varies from ~50 to ~150  
214 nm, and their length is in the sub-micrometer range. These urchin-like structures  
215 are symmetric with diameters ranging between 5–15  $\mu\text{m}$ . This initial morphology  
216 is altered in the annealed samples. From the SEM image of S-30, we observe  
217 sharper needle-like structures compared to S-22, indicating denser, well-connected  
218 features with morphology that is consistent with the phase evolution observed from  
219 XRD data. The micrographs of samples S-35 and S-40 show a somewhat mixed  
220 microstructure. The micrograph of sample S-45 shows a significant change, where

221 needle-like features disappear, and the surface appears to develop granular fea-  
 222 tures. Here, we did not detect the existence of the VO<sub>2</sub>(M) phase and instead  
 223 observe the formation of pure V<sub>2</sub>O<sub>5</sub>. In summary, SEM analysis demonstrates that  
 224 annealing temperatures strongly influence the morphological evolution of the  
 225 nanostructures, while the associated changes in crystallinity and phase composi-  
 226 tion are confirmed by XRD data.

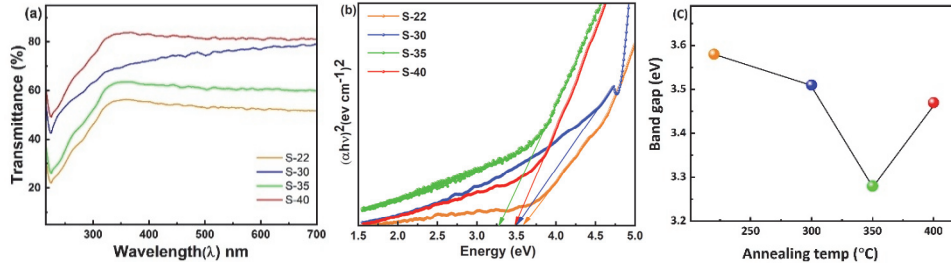
### 227 *Optical properties*

228 We performed UV–Vis spectroscopy to study the transmittance characteristics  
 229 of vanadium oxide nanostructures. We calculated the optical band gap of these  
 230 nanostructures with the help of a Tauc plot, which follows the equation:

$$231 \quad \alpha h\nu = A(h\nu - E_g)^n \quad (1)$$

232 Where  $E_g$  is the band gap,  $\alpha$  is the absorption coefficient,  $h\nu$  represents the energy  
 233 of light,  $A$  is a constant and  $n$  denotes the nature of the transition.

234 Fig. 5 illustrates the effect of various annealing temperatures on the optical  
 235 characteristics of the samples. The UV–Vis transmission spectra (Fig. 5a) indicate  
 236 that the transmittance generally increases with annealing temperature, indicating  
 237 improved crystallinity in the samples.



238  
 239 Fig. 5. a) Optical transmittance spectra of the samples annealed at various temperatures;  
 240 b) corresponding Tauc plots representing the magnitude of the direct optical band gap;  
 241 c) changes in optical band gap values with annealing temperature.

242 We calculated the direct band gap energies, from the Tauc plots in Fig. 5b, by  
 243 extrapolating  $(\alpha h\nu)^2$  versus energy ( $h\nu$ ). The plots reveal a distinct trend of  
 244 decreasing in optical band gap values with increasing annealing temperature up to  
 245 350 °C. Following this, there was a modest increase of the band gap at 400 °C.  
 246 Corresponding band gap values were calculated from the Tauc plots. As shown in  
 247 Fig. 5c,  $E_g$  decreases from 3.6 eV for sample S-22 to a minimum of 3.3 eV for  
 248 sample S-35 and subsequently increases to 3.5 eV for sample S-40. Despite the  
 249 minor morphological variations, the changes in  $E_g$  are primarily governed by phase  
 250 transitions, as observed through XRD analysis. The increased band gap in hydro-

251 thermally synthesized urchin-like VO<sub>2</sub> samples with respect to bulk VO<sub>2</sub><sup>28,29</sup> (typ-  
 252 ically 0.6–0.7 eV for the monoclinic structure) can be explained by several factors.  
 253 Nanoscale crystallite size leads to quantum confinement effects, producing a wider  
 254 band gap. Since VO<sub>2</sub>(B) was found to have a wider band gap than VO<sub>2</sub>(M), the  
 255 existence of both monoclinic (M) and metastable B phases together also contri-  
 256 butes to the wider band gap.<sup>30</sup> The lattice distortion and structural distortions also  
 257 change the electronic structure. Defects and oxygen vacancies create localized  
 258 states that change the band gap.<sup>32</sup> All these factors together are the potential  
 259 reasons behind the much broader band gap in the VO<sub>2</sub> nanostructures.

### 260 *Thermochromic properties*

261 Fig. 6 presents the differential scanning calorimetry (DSC) thermograms of  
 262 VO<sub>2</sub>(B) powders annealed at various temperatures (300–450 °C) for 30 min, with  
 263 corresponding thermal parameters summarized in Table I. The transition temper-  
 264 ature (T<sub>C</sub>) was determined as the midpoint between the endothermic peak temper-  
 265 ature during heating and the exothermic peak temperature during cooling. Samples  
 266 S-22, S-30 and S-45 do not display any prominent endothermic or exothermic  
 267 peaks in the DSC curves. The absence of a clear metal–insulator transition in S-22  
 268 and S-30 can be attributed to the dominance of the VO<sub>2</sub>(B) phase, which does not  
 269 exhibit a sharp transition like monoclinic VO<sub>2</sub>(M). In addition, broader XRD peaks  
 270 were observed for these samples, indicating reduced crystallinity. This leads to  
 271 weaker cooperative lattice distortion, which is necessary for an abrupt structural  
 272 transition. For sample S-45, the disappearance of the transition is due to the dominant  
 273 V<sub>2</sub>O<sub>5</sub> phase as identified by XRD, which does not exhibit a metal–insulator  
 274 transition in this temperature range.<sup>31,32</sup>

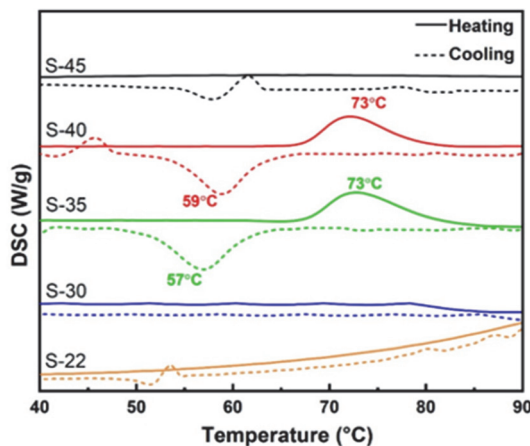


Fig. 6. DSC results illustrating a well-defined, reversible metal–insulator transition exclusively in the specimens annealed at 350 and 400 °C. In contrast, other samples exhibit a featureless thermal profile indicating the absence of a detectable phase transition.

275 For the samples S-35 and S-40, the endothermic peak maximum during the  
 276 heating cycle remains nearly constant at ~73 °C. However, the exothermic peak

277 during the cooling cycle shifts slightly from 57 °C for S-35 to 59 °C for S-40. As  
 278 a result, the calculated transition temperature ( $T_C$ , determined as the midpoint  
 279 between heating and cooling peaks) increases only slightly from 65 °C (for S-35)  
 280 to 66 °C (for S-40). Simultaneously, the thermal hysteresis width ( $\Delta T$ ), calculated as  
 281 the difference between the heating and cooling transition temperatures, decreases  
 282 from 16 to 14 °C. A reduction in the magnitude of  $\Delta T$  suggests improved rever-  
 283 sibility of the structural transformation. This behavior correlates with the enhanced  
 284 crystallinity observed in the XRD patterns of S-40 relative to S-35, implying that  
 285 improved structural ordering contributes to a more uniform and coherent phase  
 286 transition. The observed  $T_C$  values are slightly lower than those of bulk  $\text{VO}_2(\text{M})$ ,  
 287 which is typically  $\sim 68$  °C. This reduction to  $\sim 65$  °C can be attributed to residual  
 288  $\text{VO}_2(\text{B})$  and nanocrystalline interfaces. Overall, the appearance and sharpness of  
 289 the metal–insulator transition are strongly governed by phase composition and  
 290 crystallinity. Samples dominated by  $\text{VO}_2(\text{B})$  or  $\text{V}_2\text{O}_5$  do not exhibit a prominent  
 291 transition, whereas samples containing predominantly the monoclinic  $\text{VO}_2(\text{M})$   
 292 phase exhibit a distinct and reversible MIT. The improved crystallinity observed  
 293 in XRD for S-35 and S-40 contributes to a narrower hysteresis width and more  
 294 consistent structural transformation. Similar reductions in transition temperature  
 295 and broadening of the MIT in nanocrystalline or mixed-phase  $\text{VO}_2$  systems have  
 296 been reported in previous studies, where strain effects and phase heterogeneity  
 297 were found to influence MIT behavior.<sup>33–35</sup>

298 TABLE I. Comparison of phase transition temperatures obtained from DSC analysis during  
 299 heating and cooling cycles

Sample	Annealing temp. °C	Dominant phase	Secondary phase	$T_{\text{heat}}$ °C	$T_{\text{Cool}}$ °C	$T_C$ °C	$\Delta T$ °C
S-22	As-synthesized	$\text{VO}_2(\text{B})$	–	–	–	–	–
S-30	300	$\text{VO}_2(\text{B})$	$\text{VO}_2(\text{M})$	–	–	–	–
S-35	350	$\text{VO}_2(\text{M})$	$\text{V}_2\text{O}_5$ , $\text{V}_3\text{O}_7$	73	57	65	16
S-40	400	$\text{V}_2\text{O}_5$	$\text{VO}_2(\text{M})$ , $\text{V}_3\text{O}_7$	73	59	66	14
S-45	450	$\text{V}_2\text{O}_5$	–	–	–	–	–

300 The reduction in hysteresis width may be attributed to partial conversion of  
 301  $\text{VO}_2(\text{B})$  to  $\text{V}_2\text{O}_5$ , as detected by X-ray diffraction (XRD). It may also be due to  
 302 the presence of defects at the interface.<sup>34</sup> In contrast, samples S-35 and S-40 clearly  
 303 exhibit a phase transition, consistent with the phase evolution confirmed by XRD.

304 In addition, sample S-35 exhibited an average transmittance of up to about 59 %  
 305 obtained at room temperature (300 K), which is comparable to or slightly improved  
 306 compared to published literature.<sup>32,33</sup> Phase transformation in  $\text{VO}_2$  was clearly  
 307 observed for samples annealed at 350 °C, demonstrating that this procedure is  
 308 simple and energy efficient. For an observable phase transition in  $\text{VO}_2$  prepared  
 309 by reduction of  $\text{V}_2\text{O}_5$ , the required annealing temperature is often above 400 °C

310 and the annealing time is more than 1 h as reported in previous works.<sup>36,37</sup> Our  
311 method lowers the thermal budget by achieving VO<sub>2</sub> phase transformation faster  
312 (30 min) and at a lower annealing temperature than previously reported schemes.  
313 The resulting VO<sub>2</sub>(M) nanostructures exhibit reversible thermochromic behavior.

314 Integrating XRD, Raman, optical and DSC analyses indicates a distinct phase–  
315 –property correlation across the synthesized and annealed nanostructures. Spe-  
316 cimens dominated by VO<sub>2</sub>(B) (S-22, S-30) are characterized by broadened dif-  
317 fraction profiles and wider band gaps, while also lacking an observable MIT. In  
318 contrast, the formation of a predominantly VO<sub>2</sub>(M) phase at 350 °C (S-35) is asso-  
319 ciated with significant band gap narrowing and the emergence of a well-defined,  
320 reversible MIT near 65 °C. Progressive oxidation from 400–450 °C results in the  
321 formation of V<sub>2</sub>O<sub>5</sub>, which effectively suppresses this transition. These findings  
322 show that phase purity and crystallinity are major factors governing the thermo-  
323 chromic properties and MIT in these nanostructures.

324

#### CONCLUSION

325 VO<sub>2</sub> nanostructures were synthesized using a stabilizer-free hydrothermal  
326 process followed by controlled thermal annealing. The as-prepared sample (S-22)  
327 predominantly exhibited the metastable VO<sub>2</sub>(B) phase with high crystallinity.  
328 Annealing at 350 °C resulted in the formation of a predominantly monoclinic  
329 VO<sub>2</sub>(M) phase, accompanied by minor secondary phases of V<sub>2</sub>O<sub>5</sub> and V<sub>3</sub>O<sub>7</sub>. With  
330 a further increase in annealing temperature to 400 °C, V<sub>2</sub>O<sub>5</sub> became the predom-  
331 inant phase while the relative intensity of VO<sub>2</sub>(M) decreased, indicating progressive  
332 oxidation of VO<sub>2</sub>. Annealing at 450 °C resulted in the complete oxidation of VO<sub>2</sub>  
333 to V<sub>2</sub>O<sub>5</sub>. While the crystallite size increased with annealing temperature, the band  
334 gaps exhibited a non-monotonic variation with annealing temperature and phase  
335 composition. The sample annealed at 350 °C showed an average room-temperature  
336 transmittance of 59 % and a phase-transition temperature of ~65 °C. Samples  
337 S-35 and S-40 exhibit clear, reversible phase transitions between 65 and 66 °C. In  
338 summary, we demonstrate the tunability of phase composition and transition  
339 behavior in annealed VO<sub>2</sub> nanostructures and provide insight into the relationship  
340 between structural evolution and metal–insulator transition behavior. Our demon-  
341 stration of a cost-effective and stabilizer-free hydrothermal synthesis route also  
342 offers a reduced thermal budget route for scalable vanadium dioxide production,  
343 enabling controlled phase evolution and metal–insulator transition behavior in  
344 VO<sub>2</sub> nanostructures.

345 *Acknowledgements.* The authors want to acknowledge the support and facilities provided  
346 by National Institute of Technology Raipur, India. The author also wants to acknowledge the  
347 Guru Ghasidas University Bilaspur, India for granting the study leave to do Ph.D.

348

ИЗВОД

349

ХИДРОТЕРМАЛНА СИНТЕЗА И ФАЗНА ТРАНСФОРМАЦИЈА VO<sub>2</sub>(B) У VO<sub>2</sub>(M):

350

ИСТРАЖИВАЊЕ ПРЕЛАЗА МЕТАЛ–ИЗОЛАТОР

351

AISHWARYA RAJGONDA PATIL,<sup>1</sup> KRISHNA CHAITANYA SOLASA,<sup>1</sup> SOURAV KUMAR,<sup>2</sup> SHREEYA RANE<sup>3</sup>

352

И PALASH ROY CHOUDHURY<sup>4</sup>

353

<sup>1</sup>*École Centrale School of Engineering, Mahindra University, Hyderabad, India,* <sup>2</sup>*Department of Metallurgical*

354

*Engineering and materials science, IIT Indore, India,* <sup>3</sup>*Department of Physics, University of Warwick, UK и*

355

<sup>4</sup>*Mahindra University, Survey No: 62/1A, Bahadurpally, Jeedimetla, Hyderabad, Telangana 500043, India*

356

У овом раду, VO<sub>2</sub>(B) наноструктуре су синтетизоване хидротермалним путем без

357

стабилизатора и успешно конвертоване у VO<sub>2</sub>(M) на 350 °C за само 30 min. Овим поступком

358

се постиже уштеда енергије у односу на уобичајене поступке, који генерално захтевају

359

температуре више од 400 °C и трајање дуже од једног сата. Добијене VO<sub>2</sub> наноструктуре

360

са игличастим честицама су окарактерисане коришћењем различитих техника као што су

361

XRD, раманска спектроскопија, SEM и DSC како би се испитао фазни састав, морфологија

362

и карактеристике прелаза метал-изолатор. Експериментални резултати показују да се

363

VO<sub>2</sub>(B) претежно трансформише у VO<sub>2</sub>(M) након калцинације на 350 °C, са малим уделом

364

секундарних оксидних фаза. Додатно, жарење на 450 °C довело је до потпуне фазне транс-

365

формације VO<sub>2</sub> у V<sub>2</sub>O<sub>5</sub>, што указује на осетљивост VO<sub>2</sub> на температуру калцинације. Тем-

366

пература прелаза изолатор-метал је ~65 °C, што је ниже него за VO<sub>2</sub> у комаду (~68 °C),

367

што указује на модификовано понашање прелаза у наноструктурним узорцима. Ови

368

резултати показују да се хидротермално синтетисани VO<sub>2</sub>(B) може трансформисати пре-

369

тежно у VO<sub>2</sub>(M) жарењем на 350 °C током 30 min, што омогућава реверзибилни прелаз

370

метал–изолатор близу 65 °C.

371

(Примљено 1. новембра, ревидирано 16. децембра 2025, прихваћено 22. априла 2026)

372

## REFERENCES

373

1. A. B. Georgescu, A. J. Millis, *Commun. Phys.* **5** (2022) 135

374

(https://doi.org/10.1038/s42005-022-00909-z)

375

2. A. Moatti, R. Sachan, J. Narayan, *J. Appl. Phys.* **128** (2020) 045302

376

(https://doi.org/10.1063/5.0006671)

377

3. G. Ekinici, B. Özkal, S. Kazan, *ACS Omega* **9** (2024) 26235

378

(https://doi.org/10.1021/acsomega.4c02001)

379

4. A. R. Galloni, Y. Yuan, M. Zhu, H. Yu, R. S. Bisht, C.-T. M. Wu, C. Grienberger, S.

380

Ramanathan, A. D. Milstein, *Proc. Natl. Acad. Sci.* **121** (2024) e2318362121

381

(https://doi.org/10.1073/pnas.2318362121)

382

5. N. Shukla, A. V Thathachary, A. Agrawal, H. Paik, A. Aziz, D. G. Schlom, S. K. Gupta,

383

R. Engel-Herbert, S. Datta, *Nat. Commun.* **6** (2015) 7812

384

(https://doi.org/10.1038/ncomms8812)

385

6. S. Jessadaluk, N. Khemasiri, P. Rattanawarinchai, S. Rahong, A. Rangkasikorn, N.

386

Kayunkid, S. Wirunchit, A. Klamchuen, J. Nukeaw, *Jpn. J. Appl. Phys.* **58** (2019)

387

SDDE12 (https://doi.org/10.7567/1347-4065/ab0aca)

388

7. A. Ainabayev, B. Walls, D. Casey, D. Caffrey, D. Mullarkey, A. McGlinchey, A. Khare,

389

A. Tikhonov, C. Ilhan, D. Brennan, S. J. McCormack, I. Shvets, *J. Phys. Chem., C* **127**

390

(2023) 24432 (https://doi.org/10.1021/acs.jpcc.3c06057)

391

8. R. Zhang, Q. S. Fu, C. Y. Yin, C. L. Li, X. H. Chen, G. Y. Qian, C. L. Lu, S. L. Yuan, X.

392

J. Zhao, H. Z. Tao, *Sci. Rep.* **8** (2018) 17093 (https://doi.org/10.1038/s41598-018-35490-5)

- 393 9. Q. Song, J. Zhou, L. Meroueh, D. Broido, Z. Ren, G. Chen, *Appl. Phys. Lett.* **109** (2016)  
394 263902 (<https://doi.org/10.1063/1.4973292>)
- 395 10. M. Li, S. Magdassi, Y. Gao, Y. Long, *Small* **13** (2017) 1701147  
396 (<https://doi.org/10.1002/sml.201701147>)
- 397 11. M. M. Seyfour, R. Binions, *Solar Energy Mater. Solar Cells* **159** (2017) 52  
398 (<https://doi.org/10.1016/j.solmat.2016.08.035>)
- 399 12. F. Xu, X. Cao, Z. Shao, G. Sun, S. Long, T. Chang, H. Luo, P. Jin, *ACS Appl. Mater.*  
400 *Interfaces* **11** (2019) 4712 (<https://doi.org/10.1021/acsami.8b20794>)
- 401 13. D. Malarde, M. J. Powell, R. Quesada-Cabrera, R. L. Wilson, C. J. Carmalt, G. Sankar, I.  
402 P. Parkin, R. G. Palgrave, *ACS Omega* **2** (2017) 1040  
403 (<https://doi.org/10.1021/acsomega.7b00042>)
- 404 14. C. Wang, H. Xu, C. Wang, T. Liu, S. Yang, Y. Nie, X. Guo, X. Ma, X. Jiang, *J. Alloys*  
405 *Compd.* **877** (2021) 159888 (<https://doi.org/10.1016/j.jallcom.2021.159888>)
- 406 15. J. Ni, W. Jiang, K. Yu, Y. Gao, Z. Zhu, *Electrochim. Acta* **56** (2011) 2122  
407 (<https://doi.org/10.1016/j.electacta.2010.11.093>)
- 408 16. S. R. Popuri, M. Miclau, A. Artemenko, C. Labrugere, A. Villesuzanne, M. Pollet, *Inorg.*  
409 *Chem.* **52** (2013) 4780 (<https://doi.org/10.1021/ic301201k>)
- 410 17. S. Zhang, Y. Li, C. Wu, F. Zheng, Y. Xie, *J. Phys. Chem., C* **113** (2009) 15058  
411 (<https://doi.org/10.1021/jp903312h>)
- 412 18. B.-R. Jia, M.-L. Qin, Z.-L. Zhang, S.-M. Li, X.-L. Wang, M. Huang, H.-Y. Wu, Z. Chen,  
413 X. Lu, L. Zhang, X.-H. Qu, *J. Alloys Compd.* **704** (2017) 79  
414 (<https://doi.org/10.1016/j.jallcom.2017.02.046>)
- 415 19. J. Liu, Q. Li, T. Wang, D. Yu, Y. Li, *Angew. Chem. Int. Ed.* **43** (2004) 5048  
416 (<https://doi.org/10.1002/anie.200460104>)
- 417 20. K.-C. Zhou, D.-M. Cao, Z.-Y. Li, *Trans. Nonferrous Met. Soc. China* **16** (2006) 517  
418 ([https://doi.org/10.1016/S1003-6326\(06\)60090-3](https://doi.org/10.1016/S1003-6326(06)60090-3))
- 419 21. H. H. Afify, S. A. Hassan, M. Obaida, A. Abouelsayed, *Phys., E* **114** (2019) 113610  
420 (<https://doi.org/10.1016/j.physe.2019.113610>)
- 421 22. D. Alie, L. Gedvilas, Z. Wang, R. Tenent, C. Engtrakul, Y. Yan, S. E. Shaheen, A. C.  
422 Dillon, C. Ban, *J. Solid State Chem.* **212** (2014) 237  
423 (<https://doi.org/10.1016/j.jssc.2013.10.023>)
- 424 23. M. Dhananjaya, N. G. Prakash, A. L. Narayana, O. M. Hussain, *Appl. Phys., A* **124**  
425 (2018) 185 (<https://doi.org/10.1007/s00339-017-1522-0>)
- 426 24. D. Dreifus, M. P. F. Godoy, A. C. Rabelo, A. D. Rodrigues, Y. G. Gobato, P. C.  
427 Camargo, E. C. Pereira, A. J. A. De Oliveira, *J. Phys., D* **48** (2015) 445002  
428 (<https://doi.org/10.1088/0022-3727/48/44/445002>)
- 429 25. D. Surya Bhaskaram, R. Cheruku, G. Govindaraj, *J. Mater. Sci. Mater. Electron.* **27**  
430 (2016) 10855 (<https://doi.org/10.1007/s10854-016-5194-x>)
- 431 26. B. Cheng, H. Zhang, Q. Li, J. Liu, B. Liu, *Inorganics* **10** (2022) 122  
432 (<https://doi.org/10.3390/inorganics10080122>)
- 433 27. S. Zhang, Z. Zou, T. Lv, S. Li, Y. Zhang, *Int. J. Electrochem. Sci.* **15** (2020) 7203  
434 (<https://doi.org/10.20964/2020.08.05>)
- 435 28. H. W. Verleur, A. S. Barker, C. N. Berglund, *Rev. Mod. Phys.* **40** (1968) 737  
436 (<https://doi.org/10.1103/RevModPhys.40.737>)
- 437 29. K. Schneider, *J. Mater. Sci. Mater. Electron.* **31** (2020) 10478  
438 (<https://doi.org/10.1007/s10854-020-03596-0>)

- 439 30. Meenu, P. Kumar, B. S. Dehiya, *J. Nanosci. Technol.* **5** (2019) 584  
440 (<https://doi.org/10.30799/jnst.195.19050102>)  
441 31. F. Mehmood, R. Pachter, N. R. Murphy, W. E. Johnson, C. V. Ramana, *J. Appl. Phys.*  
442 **120** (2016) 191 (<https://doi.org/10.1063/1.4972038>)  
443 32. F. Arteaga-Cardona, A. P. Franco-Bacca, F. Cervantes-Alvarez, J. J. Alvarado-Gil, N. R.  
444 Silva-González, U. Salazar-Kuri, *Appl. Phys., A* **127** (2021) 159  
445 (<https://doi.org/10.1007/s00339-021-04309-y>)  
446 33. C. Xu, G. Liu, M. Li, K. Li, Y. Luo, Y. Long, G. Li, *Mater. Des.* **187** (2020) 108396  
447 (<https://doi.org/10.1016/j.matdes.2019.108396>)  
448 34. K. L. Gurunatha, S. Sathasivam, J. Li, M. Portnoi, I. P. Parkin, I. Papakonstantinou, *Adv.*  
449 *Funct. Mater.* **30** (2020) 27 (<https://doi.org/10.1002/adfm.202005311>)  
450 35. L. Liu, F. Cao, T. Yao, Y. Xu, M. Zhou, B. Qu, B. Pan, C. Wu, S. Wei, Y. Xie, *New J.*  
451 *Chem.* **36** (2012) 619 (<https://doi.org/10.1039/C1NJ20798A>)  
452 36. B. S. Beckerle, A. B. Cezar, I. T. Neckel, W. H. Schreiner, A. G. Bezerra Jr., I. L. Graff,  
453 J. Varalda, D. H. Mosca, *J. Appl. Phys.* **134** (2023) 123  
454 (<https://doi.org/10.1063/5.0169279>)  
455 37. S. A. Corr, M. Grossman, Y. Shi, K. R. Heier, G. D. Stucky, R. Seshadri, *J. Mater. Chem.*  
456 **19** (2009) 4362 (<https://doi.org/10.1039/B900982E>).